



Temperature Effects in the Composition of Metal Halide Perovskite thin Films

M. Castro-Colin^{1*}, L. Banuelos², C. Diaz-Moreno², D. Hodges³, E. Ramirez-Homs², D. Korolkov¹, N. Sharmin², and J. A. Lopez².¹*Bruker AXS, Karlsruhe, Germany*²*Dept. of Physics, U. of Texas at El Paso, El Paso, TX, USA*³*Electrical and Computer Eng. Dept., U. of Texas at El Paso, El Paso, TX, USA**Email: m.castrocolin@gmail.com

ARTICLE INFORMATION

Received: June 14, 2018

Revised: June 26, 2018

Accepted: July 15, 2018

Published online: August 6, 2018

Keywords:

Perovskites, Photovoltaic, Energy
Conversion, X-ray Reflectivity, X-ray
Fluorescence.DOI: [10.15415/jnp.2018.61007](https://doi.org/10.15415/jnp.2018.61007)

ABSTRACT

Metal halide perovskites have shown to be a structure with great promise as an efficient photovoltaic, but at the same time it is affected by instability problems that degrade their performance. Degradation mechanisms vary with temperature, moisture, oxidation, and energy conversion during light exposure. We study performance loss due to temperature by probing diffusion of elemental composition across the thickness of films produced by spin coating and for temperatures ranging from 20 to 200°C. X-ray reflectivity was used to identify the electron density, composition, and quality of the films, aided with X-ray fluorescence and X-ray photoelectron spectroscopy studies to obtain information about degradation of the organic phase of the films.

1. Introduction

Perovskite solar cells (PSC) saw their introduction to the modern world of photovoltaics as a result of research in dye sensitized solar cells [1]. The efficiency of earlier PSC was about 3% [2] and most recently have increased to about 22% [3]. Efficiencies achieved in the lab are comparable to those of commonly known Si photocells [4]. Together with their efficiency, the main advantage of PSC is the low manufacturing cost. PSC are readily manufactured with spin coating processes [5, 6]. However, such processes present scalability difficulties when compared to those employed in modern semiconductor facilities. Possibly the main hurdle with PSC are their susceptibility to degradation. The basic structure of PSC, as is well known, corresponds to the formula ABX_3 , where, in the case here presented, A = methylammonium (MAI), B = Pb, and X = I, i.e., with formulation $CH_3NH_3PbI_3$. Other combinations of materials are being researched by other groups to tune the bandgap [7] or to try to mitigate the toxicity of the compounds [8, 9]. We are addressing the effect of temperature-induced degradation only for $CH_3NH_3PbI_3$ deposited on soda-lime glass substrates. The design of the solar cells studied here was based on initial estimations [5, 6], which suggested thicknesses ranging from 150 to 500 nm. However, experimentally the

thickness started at 16 nm. The thickness is comparable to the exciton diffusion length, which is advantageous, without ignoring that photon absorbance due to thickness is an important factor. However we seek to explore efficiency of the structure on a diffusion-length-like thickness realm.

2. Materials and Methods

2.1 Sample preparation description and XPS, XRF, and XRR analyses

The samples were prepared following the next scheme:

1. Four sets of samples, each set consisting of six samples. Each sample annealed at a different temperature.
2. Each set was produced by a distinct method. there was a total of four methods:
 - a. One-step process. PbI_2 and MAI were mixed to form $CH_3NH_3PbI_3$ solution. The solution was then spin coated on soda-lime glass. Annealing took place on a hot plate at 40°C for 3 min and 100°C for 5 min. These samples were annealed at six different temperatures: room temperature, 90, 100, 130, 160, and 200°C.

- b. Two-step process. PbI_2 was spin coated on soda-lime glass, then annealed on a hot plate at 40°C for 3 min and 100°C for 5 min. Subsequently MAI was spin coated.
- c. Three-step process. Similar to the two-step method, but after MAI was spin coated, the sample was annealed by dipping into 30 mL diethyl ether.
- d. Hot cast process. A solution was made by dissolving 0.462 g of PbI_2 and 0.1589 g of MAI in 2 mL dimethylformamide (DMF) ($\text{CH}_3\text{N}_2\text{C}(\text{O})\text{H}$). The molar ratio of PbI_2 :MAI was kept as 1:1. The solution was kept at 70°C , then the solution was dropped onto soda-lime glass and heat treated at 150°C . Annealing happened at 155, 165, 175, 185, and 195°C . Each annealing temperature was applied to a different sample.

Four techniques were employed to study sample degradation: X-ray photoelectron spectroscopy (XPS), X-ray fluorescence spectroscopy (XRF), and X-ray reflectivity (XRR). The techniques are mutually complementary. An instrument PHI 5600 with a hemispherical analyzer and a source Mg K-alpha was used for XPS analyses. Prior to analysis the samples were Ar-sputtered over an area of 9 mm^2 at 25 mA and a pressure of $15 \times 10^{-3}\text{ Pa}$. During analysis the chamber was kept at about $1.3 \times 10^{-7}\text{ Pa}$. Each sample was analyzed over a surface area of about 800 mm^2 and the same take off angle of 54° . The data were analyzed with the software CasaXPS [<http://www.casaxps.com/>]. XRF analyses were carried out with a handheld instrument,

X-MET-3000 (Oxford Instruments, Abingdon, UK), Ag anode. Its detector is of the SDD type. Each sample was exposed for 5 min at air atmosphere. XRF analysis followed XPS analysis since the samples had to be at all times exposed to air, and we know that air is an additional degradation source. Quantification was accomplished with PyMCA [10] Lastly one sample—one-step processed—was measured with a custom-made reflectometer, with Cu K-alpha source, NICE² instrument at UTEP Dept. of Physics. This instrument is equipped with a detector Dectris Pilatus3R 200K-A, pixel size 0.17 mm . A reflectivity curve was obtained from successive exposures of the central line of pixels. A maximum momentum transfer Q of 0.16 \AA^{-1} was covered. To analyze the reflectivity profile we used a non-commercial software [Escape, escape-app.net].

3. Results

3.1 XPS results

Four regions were identified as the most relevant: I $3d_{5/2}$, O 1s, C 1s, and Pb $4f_{7/2}$, about 620, 533, 285, and 140 eV . Degradation dissociated the perovskite films and the spectral signatures of various lines showed changes that are indicative of bonding changes, commensurate at the surface of the film structure. Samples at four annealing temperatures were analyzed: room temperature (20°C), 90, 130 and 200°C . The general tendency of O 1s and C 1s to increase in response to the atomic concentration increase as the temperature is raised is fairly clear (Figure 1). Atomic concentration increase is less prominent for I and Pb. The curve suggests segregation of elements as the lattice distorts but with no elemental loss.

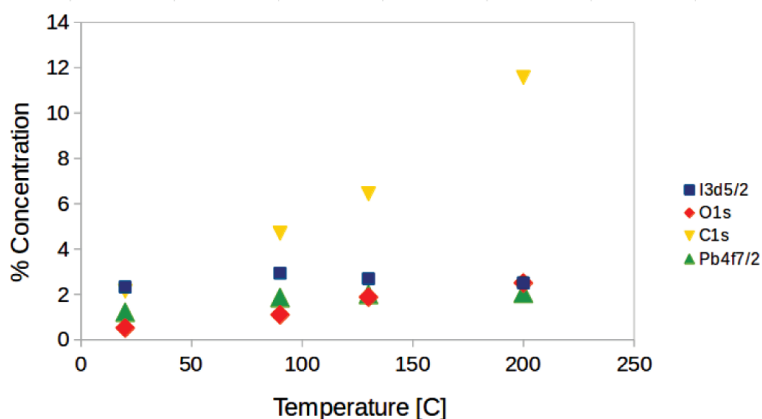


Figure 1. XPS concentration estimation at four different temperatures, one-step process sample. Four main spectral regions are quantified, I $3d_{5/2}$ (square), O 1s (diamond), C 1s (triangle down), and Pb $4f_{7/2}$ (triangle up).

The latter probably due to surface-only probing characteristic of this technique. Figure 2 gives additional details about the observation of Figure 1. There is dissociation and formation of iodine compounds, but with a steady concentration. Oxygen incorporates into the films to a larger degree, intercalating itself into the structure and forming bonds with either Pb or the organic compound (Figure 3). Likewise, carbon segregates toward the surface (Figure 4). Pb, as well as I, is not lost but rather oxidizes or simply dissociates (Figure 5) within subnanometer depths. The degree of increase of C is smaller for hot-cast processed samples compared with other samples (Figure 6). But similar to other samples, Pb and I have a steady behavior as a function of temperature. The steady behavior of I is appreciated in more detail in Figure 7. That is, the percentage concentration reduction in some species is accompanied by the increase of another, i.e., CH_3I and I_2^- are prominent.

Oxidized species are more varied with hot-cast process (Figure 8). That is also the case for C species (Figure 9). The two dominant spectral signatures in the hot-cast process are Pb and $\text{Pb}(\text{NO}_3)_2$ (Figure 10). The kinematics of degradation of the films is richer in the hot-cast process, which reflects the visual observation of the samples. Hot-cast processed samples degraded visually faster than one-step process samples, the former changed color within two weeks. The greater speed of degradation is not however accompanied by steeper percentage concentration changes possibly due to a readily unstable precursor. Tables 1 to 4 display the fitting parameters obtained during analysis. Those results were described on Figures 1 to 10, i.e. samples produced by one-step and hot-cast process at room temp and 200 °C. Four rows (bold type) indicate the main spectral components quantified for which its respective relative sensitivity factor (R.S.F) was tabulated. Spectral shifts of the main spectral components were quantified using a R.S.F. of one within their respective group.

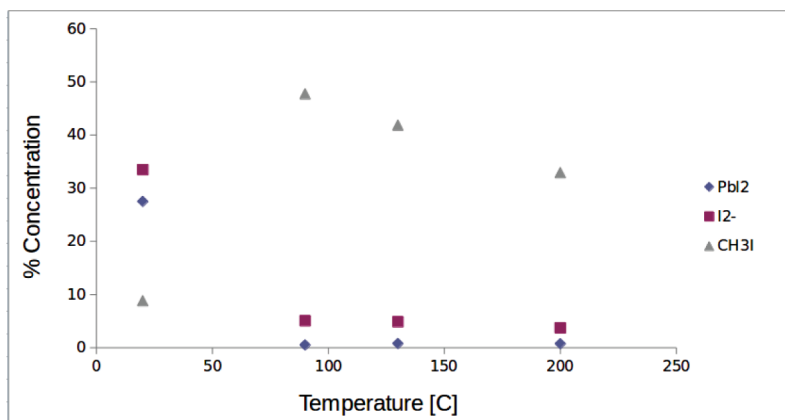


Figure 2. XPS concentration estimation at four different temperatures, one-step process sample. Three spectral shifts are represented: PbI_2 (diamond), I_2^- (square), and CH_3I (triangle up). Their respective energies are 619.501, 619.909, and 620.55 eV.

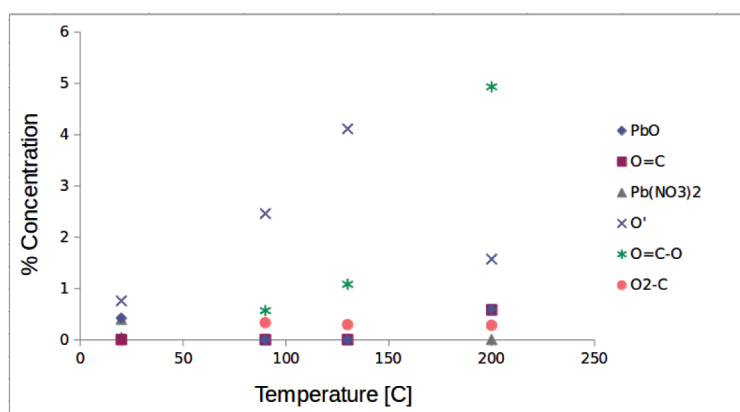


Figure 3. XPS concentration estimation at four different temperatures, one-step process sample. Five spectral shifts are represented: PbO (diamond), $\text{O}=\text{C}$ (square), $\text{Pb}(\text{NO}_3)_2$ (triangle up), O' (cross), $\text{O}=\text{C}-\text{O}$ (star), and O_2-C (circle). Their respective energies are 531.434, 532.882, 532.609, 533.600, 535.692, and 537.546 eV.

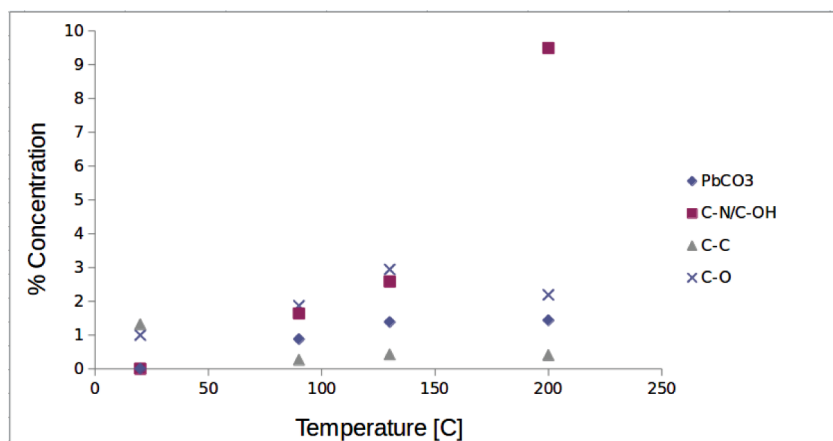


Figure 4. XPS concentration estimation at four different temperatures, one-step process sample. Four spectral shifts are represented: PbCO₃ (diamond), C-N/C-OH (square), C-C (triangle up), and C-O (cross). Their respective energies are 289.529, 287.166, 284.757, and 287.084 eV.

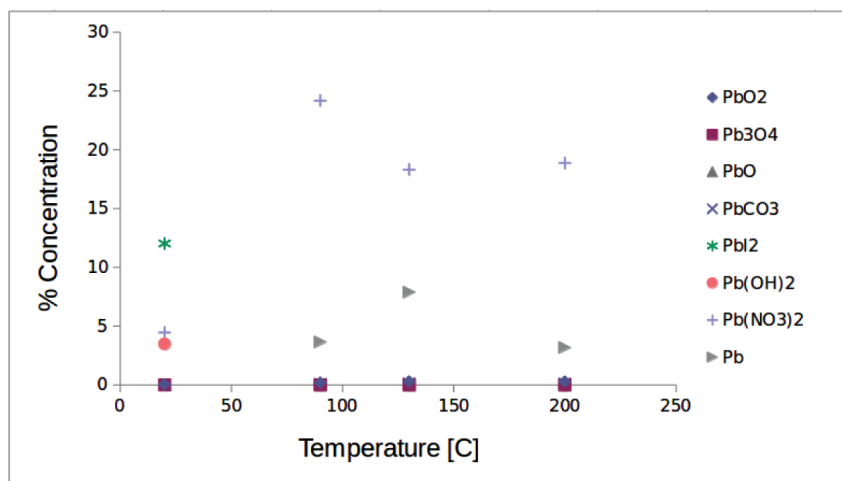


Figure 5. XPS concentration estimation at four different temperatures, one-step process sample. Eight spectral shifts are represented: PbO₂ (diamond), Pb₃O₄ (square), PbO (triangle up), PbCO₃ (cross), PbI₂ (star), Pb(OH)₂ (circle), Pb(NO₃)₂ (plus), and Pb (triangle right). Their respective energies are 137.008, 137.640, 137.784, 138.307, 138.518, 138.398, 139.589, and 141.605 eV.

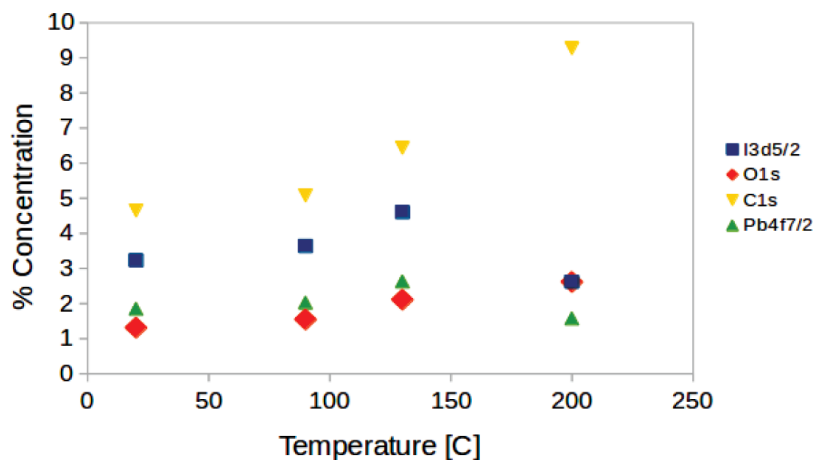


Figure 6. XPS concentration estimation at four different temperatures, hot-cast process sample. Four main spectral regions are quantified, I 3d_{5/2} (square), O 1s (diamond), C 1s (triangle down), and Pb 4f_{7/2} (triangle up).

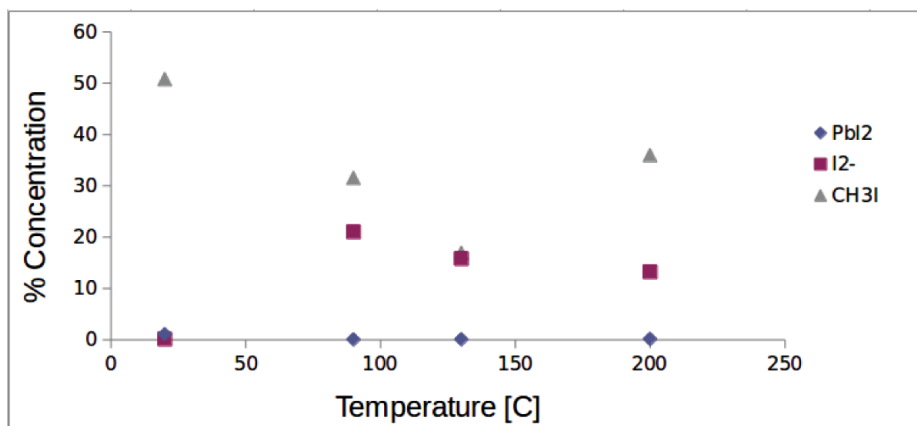


Figure 7. XPS concentration estimation at four different temperatures, hot-cast process sample. Three spectral shifts are represented: PbI₂ (diamond), I₂- (square), and CHI₃ (triangle up). Their respective energies are 619.5, 619.909, and 620.56 eV.

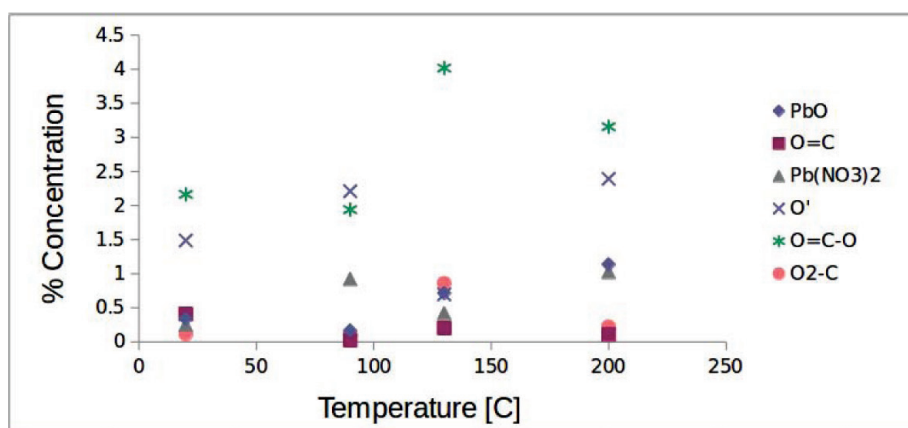


Figure 8. XPS concentration estimation at four different temperatures, hot-cast process sample. Five spectral shifts are represented: PbO (diamond), O = C (square), Pb(NO₃)₂ (triangle up), O' (cross), O = C – O (star), and O₂ – C (circle). Their respective energies are 531.446, 532.855, 532.609, 533.601, 535.692, and 537.541 eV.

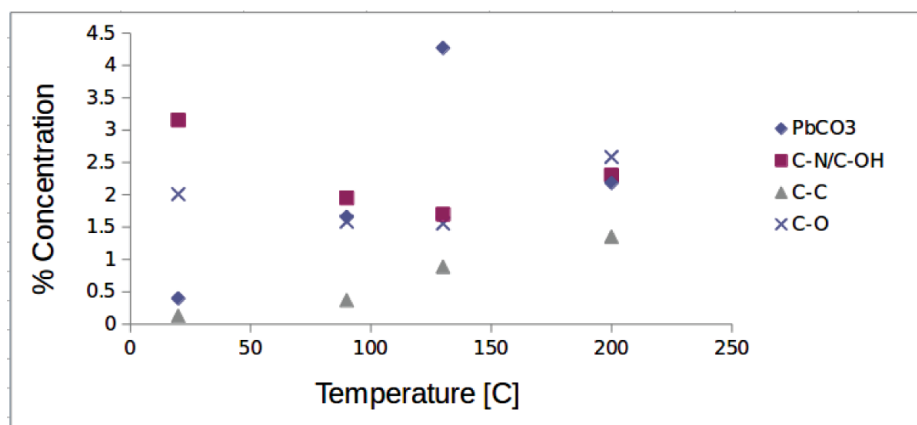


Figure 9. XPS concentration estimation at four different temperatures, hot-cast process sample. Four spectral shifts are represented: PbCO₃ (diamond), C-N/C-OH (square), C-C (triangle up), and C-O (cross). Their respective energies are 289.531, 287.165, 284.756, and 287.093 eV.

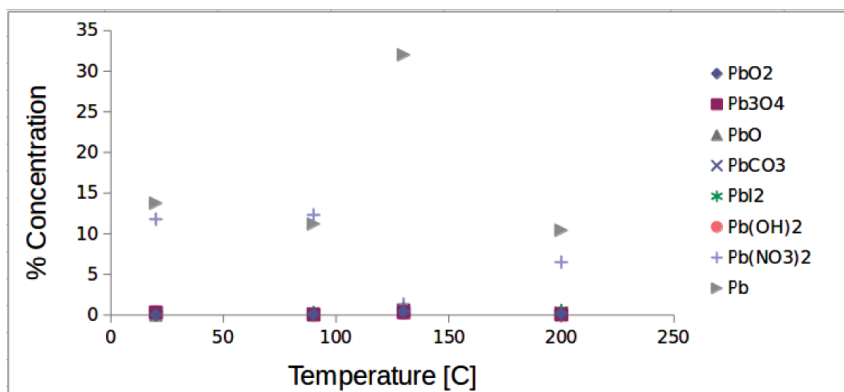


Figure 10. XPS concentration estimation at four different temperatures, one-step process sample. Eight spectral shifts are represented: PbO_2 (diamond), Pb_3O_4 (square), PbO (triangle up), PbCO_3 (cross), PbI_2 (star), Pb(OH)_2 (circle), $\text{Pb(NO}_3)_2$ (plus), and Pb (triangle right). Their respective energies are 136.940, 137.640, 137.794, 138.307, 138.510, 138.402, 139.592, and 141.607 eV.

Table 1. The results correspond to a fit of spectral components of XPS data from a one-step process sample at room temperature, 20°C. Four rows (bold type) indicate the main spectral components quantified for which its respective relative sensitivity factor (R.S.F) was tabulated. Spectral shifts of the main spectral components were quantified using a R.S.F. of one within their respective group.

Name	Position [eV]	FWHM [eV]	R.S.F.	Area [cps eV]	[%] Conc.
I 3d_{5/2}	620.000	2.837	19.3	53390.7	2.323
O 1s	533.000	3.142	2.85	1752.1	0.5163
C 1s	286.000	3.440	1	2543.4	2.136
Pb 4f_{7/2}	140.000	2.657	12.8	18541.7	1.217
PbI_2	619.501	0.477	1	32745.36	27.5
I_2^-	619.909	2.898	1	39876.61	33.49
CH_3I	620.555	0.570	1	10515.15	8.832
PbO	531.434	2.597	1	501.84	0.4215
$\text{O}=\text{C}$	532.882	1.561	1	3.8	0.003192
$\text{Pb(NO}_3)_2$	532.609	1.038	1	476.35	0.4001
O^+	533.600	2.085	1	902.96	0.7584
$\text{O}=\text{C}-\text{O}$	535.692	0.400	1	43.2	0.03628
O_2-C	537.546	5.599	1	1.5	0.00126
PbCO_3	289.529	0.794	1	4.7	0.003948
$\text{C}-\text{N}/\text{C}-\text{OH}$	287.166	3.154	1	4.7	0.003948
$\text{C}-\text{C}$	284.757	3.132	1	1573.67	1.322
$\text{C}-\text{O}$	287.084	3.543	1	1186.03	0.9962
PbO_2	137.008	2.903	1	32.5	0.0273
Pb_3O_4	137.640	2.837	1	5.4	0.004536
PbO	137.784	2.308	1	61.31	0.05149
PbCO_3	138.307	2.414	1	6.03	5.07E-03
PbI_2	138.518	2.925	1	14311.9	12.02
Pb(OH)_2	138.398	1.790	1	4132.82	3.471
$\text{Pb(NO}_3)_2$	139.589	2.938	1	5295.74	4.448
Pb	141.605	2.061	1	6	0.005039

Table 2. The results correspond to a fit of spectral components of XPS data from a one-step process sample at 200°C. Four rows (bold type) indicate the main spectral components quantified for which its respective relative sensitivity factor (R.S.F) was tabulated. Spectral shifts of the main spectral components were quantified using a R.S.F. of one within their respective group.

Name	Position [eV]	FWHM [eV]	R.S.F.	Area [cps eV]	[%] Conc.
I 3d_{5/2}	621.000	2.175	19.3	66517.5	2.502
O 1s	534.000	3.036	2.85	9815	2.5
C 1s	287.000	2.403	1	15927	11.56
Pb 4f_{7/2}	140.000	2.164	12.8	36178.8	2.052
PbI ₂	619.510	0.900	1	1000.1	0.726
I ₂ ⁻	619.916	2.038	1	5122.86	3.719
CH ₃ I	620.880	1.564	1	45380.49	32.94
PbO	531.525	3.646	1	815.29	0.5919
O=C	531.896	1.751	1	800	0.5808
Pb(NO ₃) ₂	532.590	2.417	1	5.8	0.00421
O'	535.650	2.130	1	2166.07	1.572
O=C-O	533.610	2.128	1	6794	4.932
O ₂ -C	537.812	2.429	1	385.87	0.2801
PbCO ₃	289.500	3.000	1	1979.23	1.437
C-N/C-OH	287.190	2.993	1	13073.23	9.49
C-C	284.760	1.507	1	564.91	0.4101
C-O	287.090	2.534	1	3015.26	2.189
PbO ₂	137.962	3.437	1	351.22	0.255
Pb ₃ O ₄	138.000	1.217	1	3.3	0.002396
PbO	137.980	1.757	1	1	0.0007259
PbCO ₃	138.301	2.198	1	121.98	0.08855
PbI ₂	138.431	0.836	1	167.02	0.1212
Pb(OH) ₂	138.380	0.597	1	4.99	0.003622
Pb(NO ₃) ₂	139.640	1.088	1	25993.2	18.87
Pb	141.605	1.781	1	4362.2	3.167

Table 3. The results correspond to a fit of spectral components of XPS data from a hot-cas

Name	Position [eV]	FWHM [eV]	R.S.F.	Area [cps eV]	[%] Conc.
I 3d_{5/2}	622	2.84966	19.3	52663.2	3.228
O 1s	534	3.2462	2.85	3158.7	1.311
C 1s	287	3.4236	1	3926.6	4.646
Pb 4f_{7/2}	141	2.68737	12.8	20025	1.851
Pb ₂	619.5	0.481672	1	899.2	1.064
I ₂ ⁻	619.909	0.714873	1	113.86	0.1347
CH ₃ I	620.56	0.587767	1	42930.84	50.79
PbO	531.446	2.52582	1	285.68	0.338

O=C	532.855	1.96067	1	344.26	0.4073
Pb(NO ₃) ₂	532.609	1.10576	1	212.48	0.2514
O'	533.601	1.06318	1	1254.99	1.485
O=C-O	535.692	1.39328	1	1827.82	2.162
O ₂ -C	537.541	0.933341	1	94.88	0.1122
PbC ₃ O	289.531	1.95892	1	335.12	0.3965
C-N/C-OH	287.165	2.92352	1	2666.69	3.155
C-C	284.756	3.20481	1	107.21	0.1268
C-O	287.093	3.40437	1	1697.03	2.008
Pb ₂ O	136.94	2.84037	1	8.41	0.00995
Pb ₃ O ₄	137.64	2.88042	1	255.69	0.3025
PbO	137.794	2.32701	1	16.29	0.01928
PbC ₃ O	138.307	2.44867	1	249.9	0.2956
Pb ₂	138.51	2.90952	1	52.61	0.06224
Pb(OH) ₂	138.402	1.72535	1	259.65	0.3072
Pb(NO ₃) ₂	139.592	2.09927	1	9959.36	11.78
Pb	141.607	2.17709	1	11625.1	13.75

Table 4. The results correspond to a fit of spectral components of XPS da.

Name	Position [eV]	FWHM [eV]	R.S.F.	Area [cps eV]	[%] Conc.
I 3 _{ds} /2	622	2.8361	19.3	99566.5	2.623
O 1s	535	3.19691	2.85	14651.1	2.614
C 1s	287	3.31143	1	18230.1	9.27
Pb 4 _{fp} /2	141	2.63856	12.8	39705	1.577
Pb ₂	619.491	2.94157	1	310.52	0.1579
I ₂ -	619.919	2.99674	1	26010.84	13.23
CH ₃ I	620.57	0.520833	1	70738.75	35.97
PbO	529.685	4.08067	1	2231.48	1.135
O=C	533.075	1.00872	1	211.83	0.1077
Pb(NO ₃) ₂	532.619	4.74233	1	2015.49	1.025
O'	533.607	2.3506	1	4700.71	2.39
O=C-O	535.691	2.27861	1	6204.5	3.155
O ₂ -C	538.09	0.92018	1	434.27	0.2208
PbC ₃ O	289.539	3.39763	1	4290.44	2.182
C-N/C-OH	287.199	3.06581	1	4526.86	2.302
C-C	284.758	3.40742	1	2658.01	1.352
C-O	287.119	2.17069	1	5077.09	2.582
Pb ₂ O	136.817	2.9046	1	309.23	0.1572
Pb ₃ O ₄	138.002	2.94661	1	109.04	0.05545

PbO	137.594	0.762347	1	239.09	0.1216
PbC ₃ O ₃	138.281	2.95057	1	126.78	0.06447
Pb ₂	138.509	2.95108	1	1064.5	0.5413
Pb(OH) ₂	138.419	0.600903	1	485.94	0.2471
Pb(NO ₃) ₂	139.597	1.98687	1	12789.3	6.503
Pb	141.602	1.92703	1	20489.4	10.42

3.2 XRF results

Quantification via XRF supports well the findings of XPS. XRF was only used to analyze the content of Pb and I as a function of time, between one and 52 days. Annealing temperatures of the samples ranged between 20 and 200 °C. The L lines of Pb and I were accessible with the spectrometer at hand, Pb L1, Pb L2, and Pb L3 as well as I L1, I L2, and I L3 lines. Elemental concentration of both Pb and I were quantified through fitting of the experimental profiles. Figure 11 exhibits an experimental profile and

its fit. Six spectral lines contributed to estimation of concentrations: Pb L1, Pb L2, and Pb L3 as well as I L1, I L2, and I L3, at 12.142, 12.134, 12.307, 4.371, 4.221, 4.314 keV, respectively. All six annealing temperatures were quantified similarly; however, only the lowest and highest temperatures are presented here for clarity. Only the samples annealed at room temperature presented marked changes (Figure 12). Samples annealed at 90°C already showed the same tendency observed with samples annealed at 200°C (Figure 13).

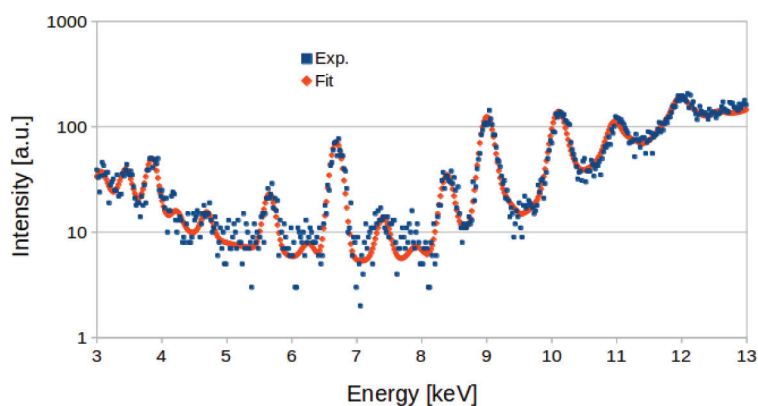


Figure 11. XRF experimental spectrum (squares) and fit (diamonds) The spectral lines of interest are Pb L1, Pb L2, and Pb L3 as well as I L1, I L2, and I L3, at 12.142, 12.134, 12.307, 4.371, 4.221, 4.314 keV, respectively.

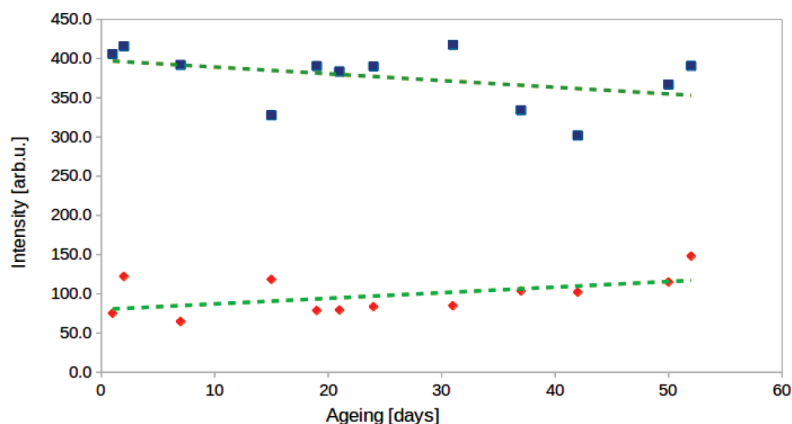


Figure 12. X-rays probe the entire film. Fluorescence from L lines of both Pb (squares) and I (diamonds) has a 98% transmission coefficient. For the samples annealed at room temperature, a trend line applied to Pb yields a 10% intensity loss, while I yields 40% intensity increase, during a time span of about 50 days.

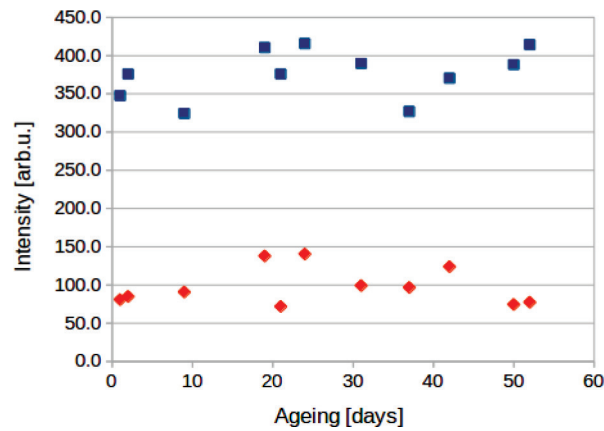


Figure 13. The samples annealed at 200°C showed a constant trend throughout the 50-day period of study. Pb (squares) and I (diamonds) show a zero-slope tendency but the counts are comparable to other temperatures.

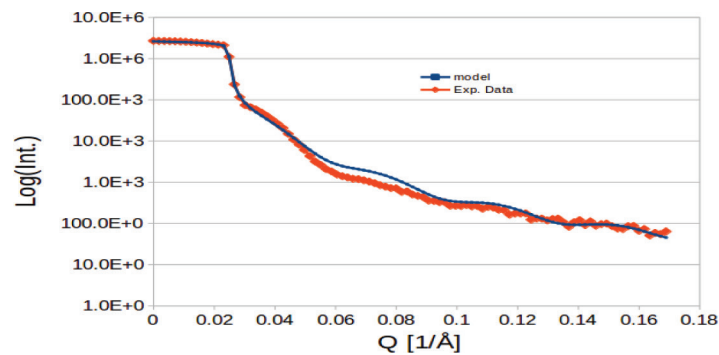


Figure 14. The one-step processed sample, annealed at room temperature, was measured with an X-ray reflectometer. A model (squares) helped us to quantify thickness, roughness electron density of the film, as well as the respective parameters of the substrate. Thickness oscillations of a 16 nm film are readily observable, indicative of a good quality film. The film had already been degraded for a period of over 50 days.

3.3 XRR results

Degradation of the samples developed to such an extent that XRR allowed us to only extract structural information from the one-step process sample annealed at room temperature. This sample had been degraded, exhibiting a yellow color after a period of more than 50 days. Despite degradation of the perovskite described by XPS and XRF, thickness oscillations were clear (Figure 14). Other samples exhibited roughness to an extent that no thickness oscillations were observed. Modeling of the reflectivity profile through a dynamical approach required only a single layer with a linearly graded electron density. The electron density of the model is represented in the standard way, $n = 1 - \delta + i(\beta)$. This approach yielded top and bottom electron densities, with $\delta = 3.622$ and 4.389×10^{-6} , respectively (Table 5). Our model has film layer thickness of 15.85 nm and a roughness of 0.18 nm. Electron density of the substrate, $\delta = 4.63 \times 10^{-6}$, corresponds well with soda

lime. Roughness of the substrate, 0.25 nm, is greater than that of the film.

Table 5. Modeling of the reflectivity curved produced the following film structural parameters.

Film	
Delta (top) [$\times 10^{-6}$]	3.622
Delta (bottom) [$\times 10^{-6}$]	4.389
Beta (top) [$\times 10^{-6}$]	-9.367
Beta (bottom) [$\times 10^{-6}$]	-3.966
Thickness [nm]	15.856
Roughness [nm]	0.1875
Substrate	
Delta (bottom) [$\times 10^{-6}$]	4.638
Beta (top) [$\times 10^{-6}$]	-2.417
Roughness [nm]	0.25

4. Discussion

The present studies favor samples annealed at room temperature manufactured with a one-step process. Structurally, the sample retained thickness and roughness quality sufficient for XRR analysis, unlike the rest of the samples. Modeling of the film may have required a graded electron density to represent the structural changes of the PSC after degradation. Oxygen intercalation expectedly diffuses from the surface into the bulk of the film, thus increasing the density down to the substrate. Our study does not include a reflectivity profile of a one-step processed sample right after deposition, and it was thus not possible to compare the structural properties of the film prior to degradation. XRR profiles were also not attained from all other samples prior to degradation, but that will be the purpose of a future study.

Elemental segregation is in agreement with XRF percentage loss of Pb intensity. Detachment of I during degradation probably enabled segregation toward the surface, via incorporation to the polymeric component. Spectral shifts of I $3d_{5/2}$ were evidenced by the increase of the spectral shift CHI_3 (Figure 2). Likewise, Pb $4f_{7/2}$ shifts to account preferentially for oxidation (Figure 5). It should be emphasized that structural information from XPS is only at the surface, and the steady concentration of Pb and I is then expected. No profile deeper into the bulk was obtained to make a comparison with the trend lines from XRF measurements. Future studies will include thickness profiles of XPS that will disclose better elemental segregation across the thickness of the film. Energy conversion efficiency has not been quantified for all samples however it is mostly relevant for one-step processed samples. We will continue research of samples with diffusion-length-like thicknesses. Additionally in subsequent studies thicknesses of at least 100 nm, are planned because they are expected to have more suitable energy conversion efficiencies. The thicknesses would correspond well with those estimated from parameters that resulted from diffusion equations and photocurrent density calculations [5]. We will also include a complete electrical efficiency characterization to provide a full description, which would require the manufacture of working solar cells.

Acknowledgements

J. A. L. acknowledges financial support from GRANT 12284027 of the US Army Research Office. The views and

opinions presented in this article are those of the author(s) and do not necessarily reflect the official views and opinions of Bruker AXS or any of its affiliates.

References

- [1] J. A. Chang, S. H. Im, Y. H. Lee, H.-J. Kim, C.-S. Lim, J. H. Heo, and S. I. Seok, *Nano Lett.*, **12** (4), 1863–1867 (2012).
<https://doi.org/10.1021/nl204224v>
- [2] M. M. Lee, J. Teuscher, T. Miyasaka, T. N. Murakami, and H. J. Snaith, *Science*, **338**, 643–647 (2012).
<https://doi.org/10.1126/science.1228604>
- [3] D. Zhao, C. Wang, Z. Song, Y. Yu, C. Chen, X. Zhao, K. Zhu, and Y. Yan, *ACS Energy Lett.*, **3** (2), 305–306 (2018).
<https://doi.org/10.1021/acseenergylett.7b01287>
- [4] NREL efficiency chart of photovoltaic cells: www.nrel.gov/pv/assets/images/efficiency-chart.png.
- [5] A. K. Misra, J. Catalan, D. Camacho, M. Martinez, and D. Hodges, *Mater Res. Express*, **4**, 085906 (2017).
<https://doi.org/10.1088/2053-1591/aa8184>
- [6] A. K. Misra, D. Hodges, and R. D. K. Misra, *Mater Res. Express*, **4**, 096201 (2017).
<https://doi.org/10.1088/2053-1591/aa86d7>
- [7] G. E. Eperon, S. D. Stranks, C. Menelaou, M. B. Johnston, L. M. Herz, and H. J. Snaith, *Energy Environ. Sci.*, **7**, 982–988 (2014).
<https://doi.org/10.1039/c3ee43822h>
- [8] R. L. Hoyer, R. E. Brandt, A. Osherov, V. Stevanovic, S. D. Stranks, M. W. Wilson, *et al.*, *Chem. Eur. J.*, **22** (8), 2605–2610 (2016).
<https://doi.org/10.1002/chem.201505055>
- [9] N. K. Noel, S. D. Stranks, A. Abate, C. Wehrenfennig, S. Guarnera, A. A. Haghighirad, A. Sadhanala, G. E. Eperon, S. K. Pathak, M. B. Johnston, A. Petrozza, L. M. Herz, and H. J. Snaith, *Energy Environ. Sci.*, **7**, 3061–3068 (2014).
<https://doi.org/10.1039/C4EE01076K>
- [10] V. A. Solé, E. Papillon, M. Cotte, Ph. Walter, J. Susini, *Acta Part B* **62**, 63–68 (2007).
<https://doi.org/10.1016/j.sab.2006.12.002>